ACS APPLIED MATERIALS & INTERFACES

www.acsami.org

Research Article

Converging Microlens Array Using Nematic Liquid Crystals Doped with Chiral Nanoparticles

Kelum Perera, Ahlam Nemati, Elizabeth K. Mann, Torsten Hegmann, and Antal Jákli*

Cite This: *ACS Appl. Mater. Interfaces* 2021, 13, 4574–4582

Read Online

ACCESS | Metrics & More | Article Recommendations | Supporting Information

ABSTRACT: Nematic liquid crystals of achiral molecules or racemic mixtures of chiral ones form flat films when suspended in submillimeter size grids and submerged under water. Recently, it has been shown (Popov et al., 2017) that films of nematic liquid crystals doped with chiral molecules adopt biconvex lens shapes underwater. The curved shape together with degenerate planar anchoring leads to a radial variation of the optical axis along the plane of the film, providing a Pancharatnam–Berry-type phase lens that modifies geometric optical imaging. Here, we describe nematic liquid crystal microlenses formed by the addition of chiral nanoparticles. It is found that the helical twisting power of the nanoparticles, the key factor to form the lens, is about 400 μm^{-1}, greater than that of the strongest molecular chiral dopants. We demonstrate imaging capabilities and measure the shape as well as the focal length of the chiral nanoparticle-doped liquid crystal lens. We show that measuring the shape of the lens allows one to calculate the helical pitch of the chiral nematic liquid crystal and thus determine the helical twisting power of the chiral ligand-capped nanoparticles. Such measurements require the use of only nanograms of chiral nanoparticles, which is 3 orders of magnitude less than that required by conventional techniques. Since NPs are sensitive to external stimuli such as light and electric and magnetic fields, the use of chiral NPs may allow the achievement of tunable optical properties for such microlens arrays.

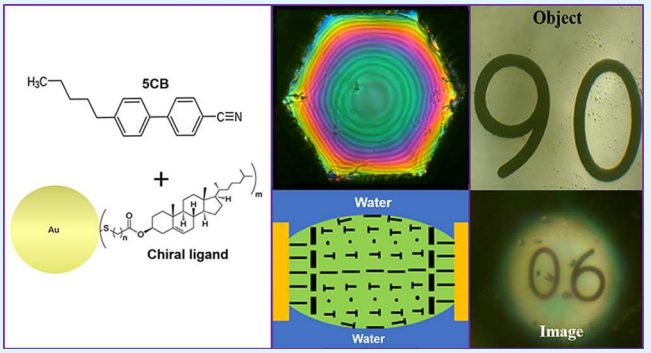

KEYWORDS: *liquid crystals, microlenses, chirality, nanoparticles, Pancharatnam–Berry phase lens, helical pitch*

INTRODUCTION

Microlens arrays are used for a wide range of applications.[1−10] Individual lenses have convex or concave spherical cap shapes where the optical path $n(r) \cdot d(r)$ varies due to the thickness variation $d(r)$, while the refractive index is constant. Fabricating such arrays usually requires complex processes such as photoresist thermal reflow,[9,10] photolithography,[11] plasmonic photopatterning,[12−14] nanoimprinting,[15] inkjet printing,[16] and direct laser writing.[17] In addition, there are flat lenses of birefringent materials where the radially varying refractive index $n(r)$ results in a bent optical path.[18−23] Another class of flat birefringent lenses are the Pancharatnam–Berry (PB) phase microlenses[12,24−31] with optical axes varying radially in the plane normal to the light.

Liquid crystals (LC) can also be used to create lenses either by filling[32] or imprinting LCs in curved substrates,[33,34] by creating focal-conic defects in smectics[35−37] or by using short helical pitch cholesteric liquid crystal polygonal textures.[38] Recently, Popov et al.[39] have shown that chiral nematic liquid crystal (N*-LC) mixtures produced by the addition of a chiral molecular dopant to an achiral N-LC, suspended in submillimeter size grids, can spontaneously form biconvex microlenses upon immersion under water. The degenerate planar anchoring caused by the water rotates the director radially as the thickness changes. This is similar to the radial variation of the Pancharatnam–Berry (PB)-type phase lens, making the free-standing cholesteric liquid crystal lens effectively an integrated PB and dynamical phase lens.[40] The combination of a pseudolayered structure of the N*-LC mixture and the elastic energy needed for unwinding the helix near the TEM grid, which promotes uniform perpendicular alignment to the wall, provides the pressure difference needed for the formation of the lens. The positive energy created by the unwinding of the helix near the wall is balanced by reducing the thickness of the LC film near the wall. Remarkably, the curvature radius of the chiral LC lens is proportional to the square of the helical pitch, which can be tuned by the chiral dopant, temperature, and even with UV light irradiation, as shown recently by Li et al.[41] Interestingly,

Received: November 25, 2020
Accepted: December 22, 2020
Published: January 7, 2021

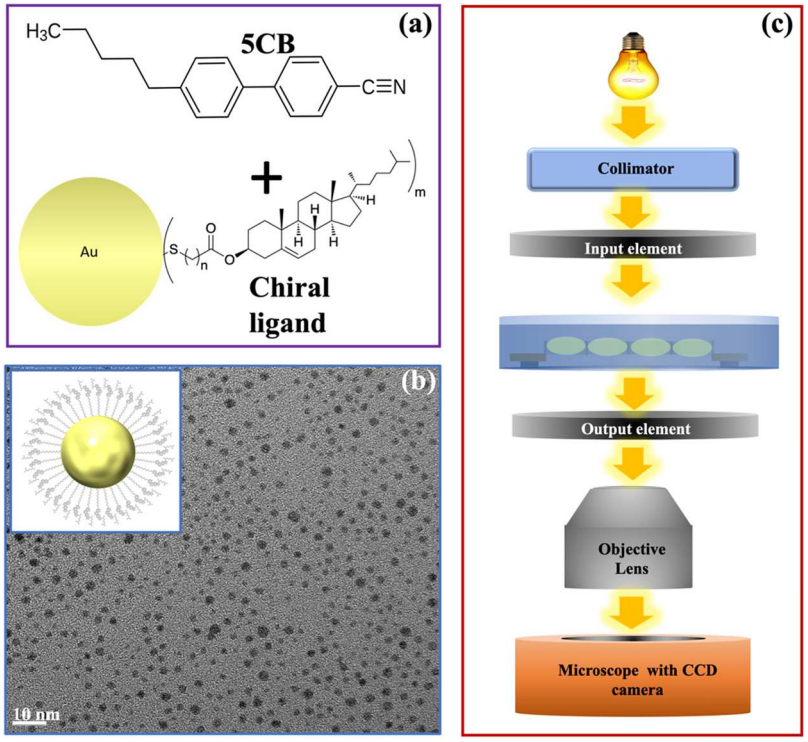

Figure 1. Materials and experimental setup used to prepare and study microlens arrays formed by chiral Au-NP-doped nematic liquid crystal 5CB. (a) Molecular structure of 5CB and the chiral ligand-capping Au NPs. (b) TEM image indicates that the average diameter of the Au NPs is about 3 nm. The inset in the upper left-hand corner shows the schematic of the Au NPs. (c) Full optical setup includes an inverted microscope equipped with a CCD camera for image acquisition. The LC sample suspended in TEM grids is placed in a glass container filled with water between input and output elements. The input element is either nothing, a linear polarizer, or left/right circular polarizers. The output element is a linear polarizer oriented 90° with respect to the input linear polarizer and is inserted only when the birefringence color of the LC lens is viewed.

such a spontaneously formed lens strongly resembles the radially varying optical axis of the compound eye of insects, such as the corneal lens structure of firefly compound eyes.[42−44] This similarity suggests that the chirality of the chitin and the aqueous environment may also be important in the formation of the compound eyes.

The addition of nanomaterials to nematic liquid crystals (NLCs) can modify the fundamental properties of NLCs. Ferroelectric nanoparticles (NPs) can increase dielectric anisotropy[45,46] and with multiferroic bismuth ferrite particles, one can achieve improved electro-optic responses.[45,47,48] The elastic properties and rotational viscosity can also be altered by adding Au NPs[49,50] and Ag NPs[51] to N-LCs. Experiments on the chirality transfer from chiral nanostructures as chiral dopants to N-LCs indicated that chiral ligand-capped Au NPs outperform their organic molecular counterparts, inducing tighter helical pitch (p) values at lower overall concentrations of the chiral molecules. In addition, such Au NPs perform this amazing feat consistently over larger distances, translating into larger chiral correlation lengths.[52,53] Such an enhancement of through-space chirality found support from recent examples of demonstrated long-range interactions between chiral molecules and plasmonic nanostructures[54] as well as enhanced anisotropy (or Kuhn's dissymmetry) factors, g ($g = \Delta\varepsilon/\varepsilon$, where $\Delta\varepsilon$ and ε are the molar circular dichroism and molar extinction coefficient, respectively) for chiral molecules in the vicinity of plasmonic nanostructures.[55,56] Recent experimental data provided additional evidence for the hypothesis that desymmetrization of a plasmonic nanostructure (substituting Au NPs for gold nanorods, GNRs) results in further through-space chirality enhancement. Here, chiral cholesterol-capped GNRs showed an aspect ratio-dependent chirality amplification, prompting their own helical assembly in the induced N*-LC host that was explained by a chiral feedback loop.[57]

Here, we describe the fabrication of spontaneously forming converging microlens arrays using NLCs doped with chiral ligand-capped Au NPs. We determine the shape, magnification, and focal length of the microlens array. Similar to molecularly doped chiral nematics, these microlens arrays work as a unique combination of geometric lens and spontaneously formed (PB) phase microlens.[39,41] From the measured optical properties, we can determine the helical twisting power (HTP) with 3 orders of magnitude less chiral materials than any other methods. It is found that the HTP of these chiral nanoparticles is several times larger than the strongest molecular chiral dopants.[53,57]

MATERIALS AND METHODS

The molecular structure of the chiral ligand (Chole-thiol) attached to the Au NPs and the structure of the liquid crystal host 4-cyano-4′-pentylbiphenyl (5CB) are shown in Figure 1a. The host 5CB was purchased from Merck and was used without further purification.

For the preparation of the cholesterol-thiol capped Au NPs, the cholesterol-thiol ligand *Chole-thiol* (0.13 mol) was added to $HAuCl_4 \cdot 3H_2O$ (0.15 mmol) dissolved in 5 mL of freshly distilled tetrahydrofuran (THF) under flowing N_2. The mixture was stirred for 30 min (700 rpm), and then $NaBH_4$ (0.76 mmol) dissolved in 5 mL DI water was added and the color rapidly changed to brown. The reaction mixture was stirred overnight. The solvent was removed under reduced pressure, and then the brown precipitate was dissolved in *iso*-propanol/chloroform = 19:1 and centrifuged (12,000 rpm, 15 min) twice. The solvents were removed under reduced pressure, and the particles were dried under N_2. The NPs, redispersed in

https://dx.doi.org/10.1021/acsami.0c21044
ACS Appl. Mater. Interfaces 2021, 13, 4574−4582

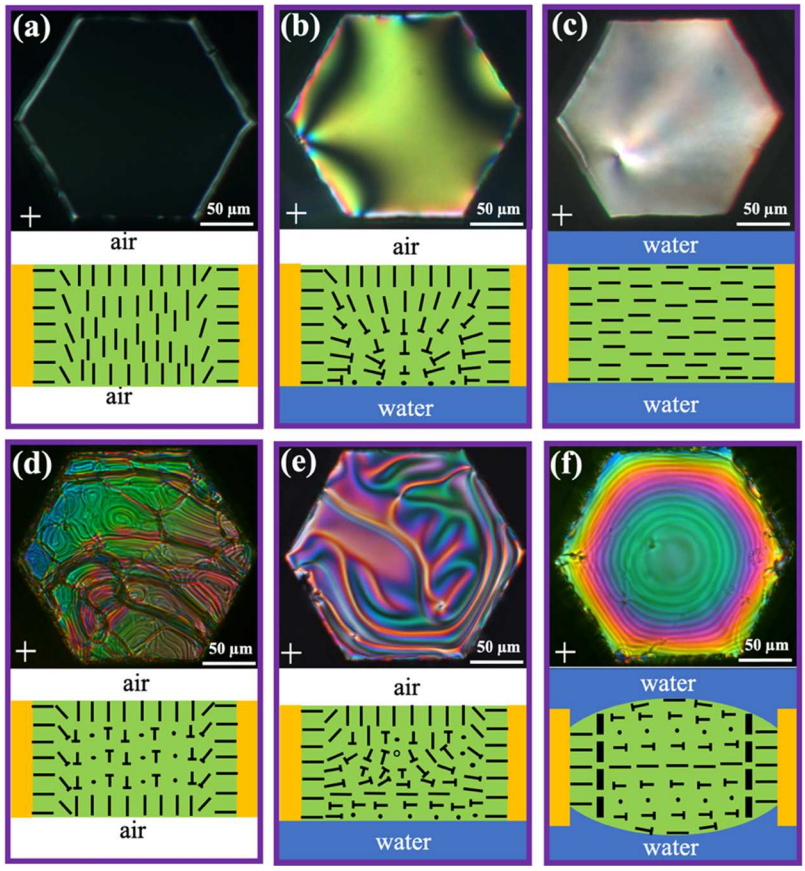

Figure 2. POM images of nematic liquid crystal (NLC) films viewed between crossed linear polarizers (in directions shown by white crosses) under white light illumination and below the sketches of the side view of their director structures when suspended in hexagonal TEM grids between air−air (a, d), air−water (b, e), and water−water (c, f) interfaces. (a−c) Achiral NLC (pure 5CB) and (d−f) 5CB mixed with 0.2 wt % chiral Au NPs.

dichloromethane, were mixed with different concentrations of 5CB under N_2 at room temperature for 48 h. The synthesis of the chiral ligand was accomplished according to previously reported methods.[53] Figure 1b shows the transmission electron microscopy (TEM) image of the chiral ligand-capped Au NPs with an average diameter of 3 nm diameter chiral nanoparticles taken with an FEI Tecnai TF20 TEM instrument at an accelerating voltage of 200 kV.

Mixtures with 0.05−0.3 wt % of Au NPs were prepared by following standard protocols. Precise quantities were weighed into rigorously cleaned glass vials using an ultramicrobalance. Standardized solutions of each chiral additive and NLC host in a purified organic solvent (chloroform $CHCl_3$) were prepared, and the desired volumes of each solution were combined, using calibrated Eppendorf pipettes, and thoroughly mixed. Thereafter, the solvent was evaporated under nitrogen at room temperature over a period of 48 h.

The resulting N-LC mixtures were suspended in nickel 50/100 mesh Veeco folding nickel TEM grids (Ted Pella Inc.). The grids are 20 μm thick and have hexagonal shape with 100 μm edge length. A Branson B200 ultrasonic cleaner was used to clean the grids in methanol and dried using a stream of air before use. The mesh was carefully placed on top of a glass slide with a rectangular opening. The TEM folding grid containing two halves was held by one empty half while the other half ("sample part") contained the suspended LC films. The width of the opening was slightly smaller than the diameter of the TEM grid so that the TEM grid could rest on top of the opening without falling. Two pieces of tape were used to secure the grid firmly to the glass slide. Using a micropipette, a small drop of LC mixture was carefully placed on top of the grid so that it could evenly spread on the mesh and make a uniform LC film. The TEM grid was held inside a glass dish (height: 10 mm) at about 5 mm from the bottom using two rectangular clamp holders. The dish was carefully filled with ultrapurified water (18.2 MΩ cm) obtained from the PureLab Plus system.

For measuring the imaging capabilities of the microlens array, a microscope calibration slide was fixed in a micropositioner, lowered until the slide touched the water surface of the glass dish and adjusted carefully until the inverted image of one of the markings in the calibration glass slide became visible on the other side of the microlens array. All photomicrographs were captured using an Olympus CK40 inverted polarizing optical microscope. The mounted CCD camera (QICAM Fast1394) enables the capturing and recording of the video in real-time. The experimental arrangement to observe the microlens array is illustrated in Figure 1c. The light blue color medium in the sketch illustrates water.

RESULTS AND DISCUSSION

Polarized optical microscopy (POM) images between crossed linear polarizers and sketches of the side view of the corresponding director structures are shown in Figure 2 for both the pure achiral 5CB and the mixture of 5CB + 0.2 wt % Au NP-capped cholesterol-thiol molecules under various boundary conditions.

The POM and the sketch of the director structure of pure 5CB film suspended in air is shown in Figure 2a. Both the air and the nickel sidewalls of the TEM grid align the director normal to the interfaces (homeotropic anchoring), resulting in dark textures everywhere except for about 20 μm region near the sidewall. This is because the director is vertical everywhere, except near the D = 20 μm thick sidewalls, where it is horizontal. When the bottom of the film is in contact with

https://dx.doi.org/10.1021/acsami.0c21044
ACS Appl. Mater. Interfaces 2021, 13, 4574−4582

water that provides degenerate planar alignment (the director is parallel to the interface without a preferred direction within the plane) and the top is in air, a hybrid alignment appears that has fourth-order greenish birefringent color far from the sidewall and third-order pinkish color near the wall (see Figure 2b). When the film is fully immersed in water (planar anchoring both at the top and at the bottom interface), the LC film shows uniform ~sixth-order color, indicating uniform film thickness (Figure 2c). These textures and their optical appearances have been discussed in the literature.[58−60]

Typical POM images and side views of the corresponding director structure are shown for air−air, air−water, and water−water interfaces of 5CB with 0.2 wt % chiral Au NPs, as shown in Figure 2d−f. The fingerprint texture seen in the air−air interface sample is shown in Figure 2d. A "ripple-like" fingerprint texture is seen in the hybrid alignment when the chiral nematic film is in contact with water and air (Figure 2e). When the chiral N-LC film is fully immersed under water, concentric colored rings appear, as shown in Figure 2f. The background birefringence color varies from second-order yellow at the edge to third-order emerald green in the middle. This color change is overlaid by about 13 dark fringes that are visible even without polarizers. This ring pattern is very similar to that formed in molecularly doped chiral NLCs, thus indicating the lens shape of the suspended film.

The fringes become more visible and sharper when a green filter (see top-right inset to Figure 3) is used with polarizers.

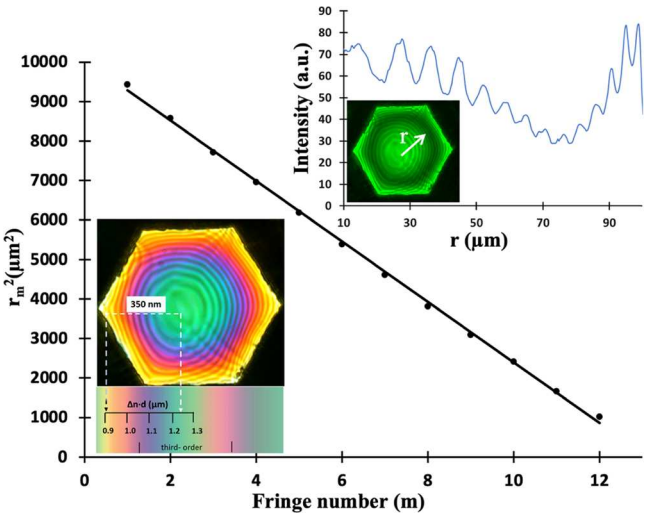

Figure 3. Analysis of the radius of curvature of the microlens with 5CB + 0.2 wt % Au NPs. The inset in the upper right-hand corner shows the intensity profile of the lens along the white arrow measured between circular polarizers with a green filter. The plot shows square distance to the intensity minima by counting m = 1 from the outermost dark ring. The inset in the bottom left-hand corner with a color scale bar shows the optical path difference of the lens based on the background color variation of the lens. The variation of the optical path difference is about 350 μm.

This allows plotting the fringe position r_m with respect to their cardinal number m counting from the edge toward the center. The fringes (Newton rings) are due to the interference between the light reflected at the bottom and top of the LC film.

For a biconvex lens with volume $a^2\pi D$, the relation between "r_m" versus "m" is given by the formula $r_m^2 = R(D + h) - \frac{\lambda R}{2n}\left(m + \frac{1}{2}\right)$, where R and h are the curvature radius and the height of the spherical cap, respectively; D is the thickness of the grid (Figure 4b); n is the refractive index of the lens ($n \approx n_e \approx 1.7$); and λ is the wavelength of the light passing through the green filter (λ = 0.55 μm). Indeed, Figure 3 shows that $r_m^2(m)$ is proportional to m with a negative slope. The slope of the r_m^2 (m) plot provides $\frac{\lambda R}{2n}$ = 766 μm^2, which gives R = 4.7 mm. The curvature ratio can also be estimated from the radial variation of the birefringence color, as shown in the bottom-left inset of Figure 3. The estimated optical path difference $\zeta = \Delta n \cdot \Delta D$ is about 350 nm. Assuming uniform birefringence Δn = 0.15, the variation of the film thickness $\Delta D \sim 2.3$ μm. $\Delta D = 2h$, where $h \sim 1.15$ μm is the height of the spherical cap, i.e., much smaller than the radius a = 100 μm of the lens. Therefore, the curvature radius R can be approximated as $R = \frac{a^2}{\Delta D} \sim$ 4.3mm. This is in good agreement with the value we obtained from the slope of the r_m^2 (m) plot.

The number of rings N and the variation of the birefringence color increase with an increase in the concentration of the chiral nanoparticles, as shown in Figure 4a. The focal lengths of these lenses were found to vary between 0.5 mm at 0.3 wt % Au NPs to 10 mm at 0.03% Au NPs, in agreement with the dependence of the focal length on the number of fringes N as[61] $f = a^2/(2N\lambda)$. This shows that the height of the spherical cap increases, and the curvature radius decreases with an increase in NP concentration. The optic ray tracing of the biconvex LC lens and the geometry of the lens are illustrated in Figure 4b. The pictures of the object (a number "90") together with its inverted image for a 0.2 wt % Au NP LC lens are shown in Figure 4c.

The focal length of the optical system can be calculated by measuring the object distance (l_o) and image distance (l_i) without the use of any polarizer. To focus on the lens, object, and image, the objective lens of the microscope moved to different positions that were calibrated to calculate l_o and l_i. In the case of the 0.2% chiral NP LC mixture for l_o = 4.49 mm, l_i = 2.64 mm was found. The magnification determined by the ratio of the image distance and object distance is $M = \frac{l_i}{l_o} = 0.6$. Within the error of the measurements, this magnification was in agreement with that found by directly comparing the image and object sizes from Figure 4c.

From geometric optics, the measured image and object distances can also provide the focal length as $f = \frac{l_o l_i}{(l_o + l_i)} = 1.67$ mm. The focal length of an isotropic lens with a uniform refractive index can also be determined from the curvature radius R of the biconvex lens. Since the specific weight of N-LC and water are almost the same, the biconvex lens should be symmetric, i.e., both the top and bottom spherical caps have the same curvature radius. Taking into account that the thickness of the lens $D \sim 20$ μm is much smaller than its aperture ($2a$ = 200 μm), we can approximate the Lensmaker equation as $\frac{1}{f_{bc}} = \left(\frac{n_{LC} - n_w}{n_w}\right)\frac{2}{R}$, where the subscript "bc" in f_{bc} refers to the biconvex shape of the lens. Due to the planar alignment, the refractive index of the LC lens is $n_{LC} \approx n_e \approx 1.7$ and the refractive index of the surrounding water is n_w = 1.33. With these and the measured R = 4.7 mm (see Figure 3), we obtain f_{bc} = 8.45 mm. This value is about 5

https://dx.doi.org/10.1021/acsami.0c21044
ACS Appl. Mater. Interfaces 2021, 13, 4574−4582

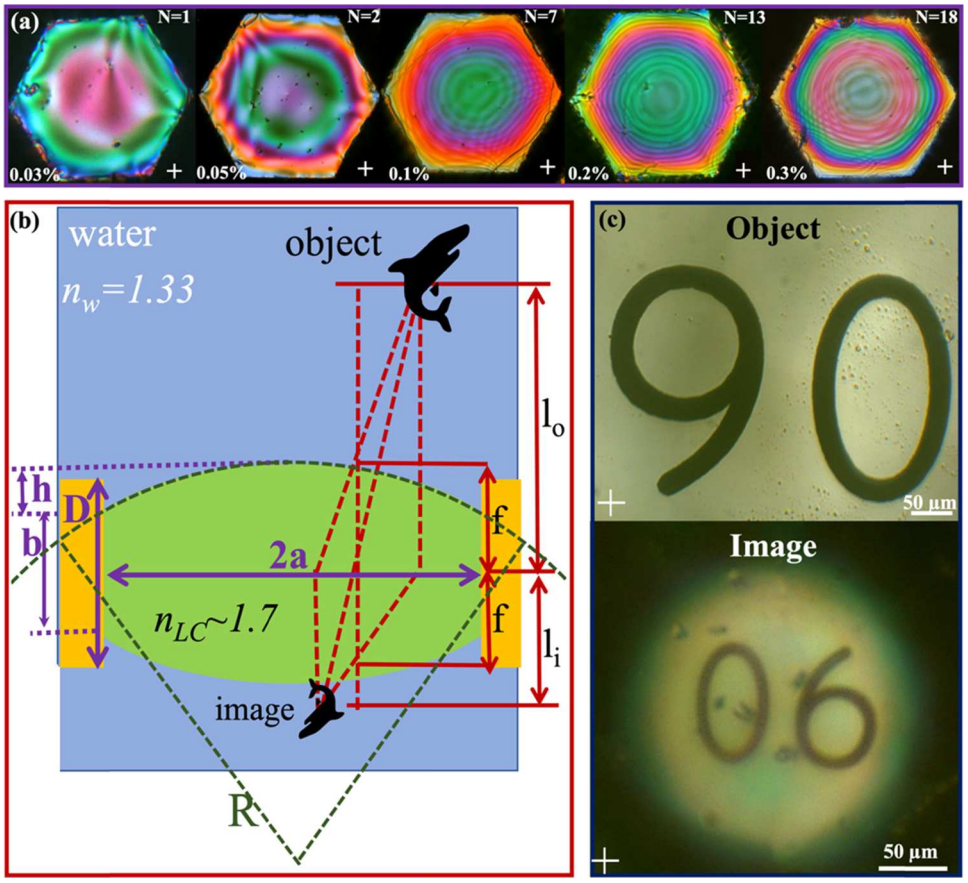

Figure 4. Illustration of the optics of Au-NP-doped LC lenses. (a) POM images of lenses with various concentrations between 0.03 and 0.3 wt % chiral NPs. The numbers on the bottom-left and top-right of each picture show the concentration and the number of fringes, respectively. (b) Optical ray tracing of the biconvex LC lens and the geometry of the lens. (c) Pictures of the object (number "90") together with its inverted image for a 0.2 wt % Au NP LC lens.

times greater than the value we calculated using the measured object and image distances. This discrepancy is similar to that observed in the molecularly doped chiral LC lenses[39] and where it was attributed to the degenerate planar anchoring at the water interface, leading to the radial rotation of the director, as shown in Figure 5a. This radial variation of the optic axis is similar to that of the Pancharatnam–Berry (PB)-type phase lenses with a constant half-wave plate thickness. At a normal light incidence on a flat PB lens immersed in a medium with refractive index n, the variation of the azimuth angle β from the center to the edge of the lens can be expressed as $\beta = \frac{2\pi}{n\lambda}(\sqrt{f_{PB}^2 + a^2} - f_{PB})$,[62,63] where λ is the wavelength of the monochromatic light, a is the radius of the lens, and f_{PB} is the focal length of the flat PB lens. After some algebraic calculations, we obtain $f_{PB} = \frac{\pi a^2}{\beta\lambda n} - \frac{\beta\lambda n}{4\pi^2}$. Since the director rotates by π when the thickness changes by $p/2$, $\beta = \frac{2\Delta D}{p}\pi = \frac{2h\pi}{p}$, giving that $f_{PB} = \frac{a^2 p}{4h\lambda n} - \frac{h\lambda n}{\pi p}$. Since the height of the spherical caps h is much smaller than the radius a and $p > \lambda$, furthermore utilizing that $a^2/2h \approx R$, we obtain $f_{PB} \approx \frac{R \cdot p}{2\lambda n}$.

To measure the pitch, we have prepared a $d = 7.5$ μm thick contact cell between the pure 5CB and 5CB doped with $c = 0.1$ wt % NP. As shown in Figure 5b, there are seven bands corresponding to regions with decreasing pitch from infinite to

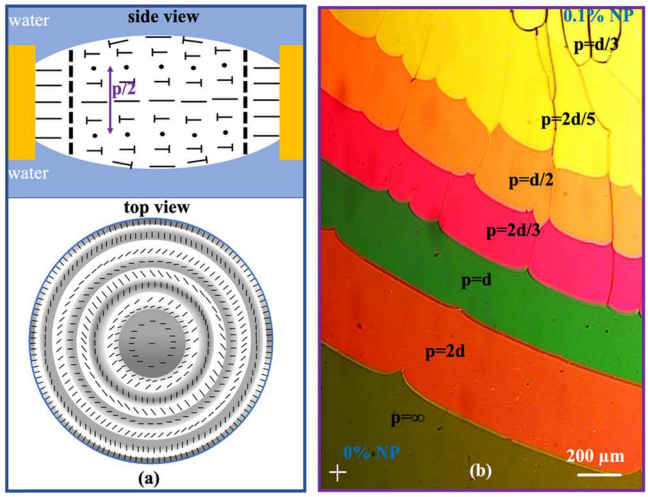

Figure 5. (a) Side and top views of the director structure of chiral nematic liquid crystal in lens-shaped droplets. The director rotates both along the film thickness and radially away from the center of the lens. (b) POM image of a 7.5 μm contact cell filled with pure 5CB from the bottom left and with 5CB + 0.1 wt % Au NPs from the top-right corner. The bands with different colors correspond to varying helical pitch that decreases from infinity at 0% NP to $p = d/3 = 2.5$ μm at 0.1 wt % NP.

$p = d/3 = 2.5$ μm. Since $p = 1/(\mathrm{HTP} \cdot c)$ where HTP is the helical twisting power, which is independent of the

https://dx.doi.org/10.1021/acsami.0c21044
ACS Appl. Mater. Interfaces 2021, 13, 4574–4582

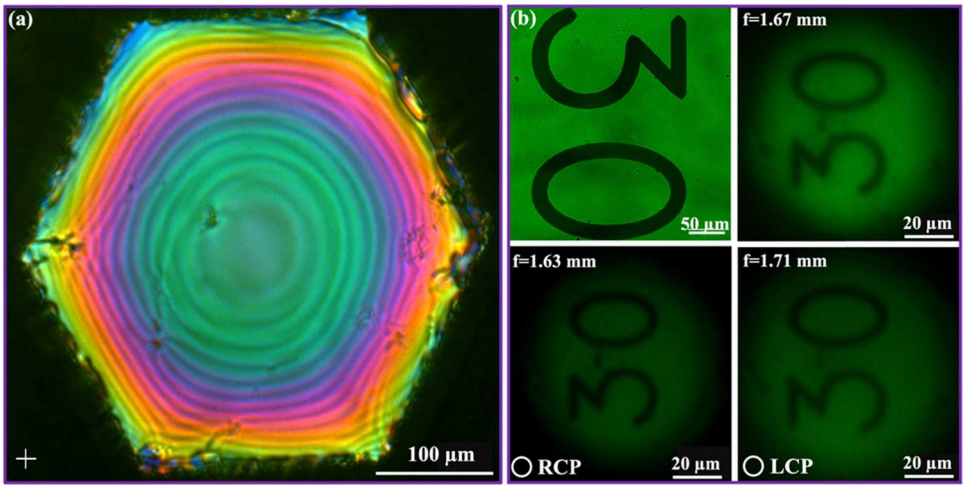

Figure 6. Imaging properties of a 0.2 wt % Au NP-doped LC lens with different polarization states. (a) Texture of the 0.2 wt % Au NP-doped LC lens between crossed polarizers (same as shown in Figure 2f). (b) Top-left: Picture of the object; top-right: picture of the image seen without polarizers; bottom-left: picture of the image seen between right circular polarizers; bottom-right: picture of the image seen between left circular polarizers.

concentration, for $c = 0.2$ wt % NP mixture $p \sim 1.25$ μm. With this pitch value, $R = 4.7$ mm, $\lambda = 0.55$ μm, and $n = n_w = 1.33$, we obtain $f_{PB} \approx 4$mm. Approximating such a lens as an integrated PB phase and a biconvex lens,[40] the focal length f can be determined by $f = f_G \cdot f_{PB}/(f_G + f_{PB})$, providing $f = 2.7$mm. This is still about 1 mm larger than the measured focal length. This difference could be attributed to two factors: (a) In calculating the radial rotation of the director, β we assumed that linearly polarized light is propagating through the cholesteric LC (Maugham limit), which, however, is only true if the cholesteric pitch is much larger than of the wavelength of the light ($p > \lambda$). In our case, the pitch is 1.25 μm; hence, the propagating light is elliptical, and the approximation is not quite good. (b) The structure of our lens is much more complicated than an integrated lens of an isotropic biconvex lens and a flat PB lens with a uniform director along the film thickness.

To verify if there is any property of the cholesteric liquid crystal lens that resembles PB phase elements, we have studied the imaging properties of the 0.2 wt % Au-NP-doped LC lens without polarizers, with linearly polarized, right- and left-hand circularly polarized inputs. PB phase elements can distinguish two circularly polarized components, as two circular polarization beams emerging from the element usually have conjugate wavefronts.[64] Therefore, the focal length of an integrated PB phase element and a convex lens will be different for left and right circularly polarized inputs as[40]

$$f_{\pm} = \frac{|f_{PB}^{\pm}| f_{bc}}{f_{bc} \pm |f_{PB}^{\pm}|}, \tag{1}$$

where + (−) represent the right (left) circularly polarized beam input. As seen in Figure 6b and in the Supporting video, we found that the focal length for linearly polarized or nonpolarized inputs is the same ($f_o = 1.67$ mm), whereas for the left and right circularly polarized inputs are $f_+ = 1.63$ mm and $f_- = 1.71$ mm. This qualitatively agrees with the prediction that an integrated PB and biconvex lens has different focal lengths for left and right circularly polarized input, as given in eq 1. However, with $f_{bc} = 8.95$ mm calculated from the shape of the lens, we obtain different values for $|f_{PB}^{+}|$ (2.1 mm) and $|f_{PB}^{-}|$ (1.4 mm). This confirms our previous assessment that the radial variation of the optical axis due to the varying thickness and degenerate anchoring has an impact on the focal length similar to that of an integrated PB phase element and biconvex lens, but the actual structure is more complicated. Future theoretical studies will be needed to determine the precise focal length of chiral nematic microlenses characterized by the spatially varying film thickness and director structure.

The measured pitch of $p \sim 2.5$ μm at $c = 0.1$ wt % also allows us to estimate the helical twisting power of the chiral nanoparticles as HTP $= (cp)^{-1} \sim 400$ μm^{-1}. This value is several times larger than the HTP of the strongest molecular chiral dopants and is the same order of magnitude as those observed for CTAB-capped gold nanorods.[53]

We note that the HTP can also be determined from the curvature radius $R \approx a^2/2h$ of the chiral NP-doped lens by utilizing the relation between h of the spherical cap and the helical pitch of the N*-LC. As calculated by Popov et al.,[39] $h \approx \frac{3\pi^2 K_{22} aD}{\gamma p^2(\pi+6)}$, where $a = 100$ μm and $D = 20$ μm are the radius and thickness of the grid, respectively; $K_{22} \sim 5$pN is the twist elastic constant; and $\gamma \sim 10^{-2}$ N/m[39] is the water LC interfacial tension. Knowing all these parameters, we can calculate the pitch as

$$p = \sqrt{\frac{3\pi^2 K_{22} aD}{\gamma h(\pi + 6)}} \tag{2}$$

From the measured height $h \sim 1.1$ μm, we obtain $p \sim 1.4$ μm, which is very close to that measured with 15% precision by us using contact cells. Importantly, such a measurement requires only filling one grid of volume $V = 3a^2D$ with 0.1 wt % NP, corresponding to less than 1 ng of the Au NPs. This is at least 3 orders of magnitude smaller than other conventional methods, such as Grandjean-Cano wedge or the ones that contact cells require. Alternatively, using chiral NPs with known HTP, eq 1 can also be used to measure either the twist elastic constant or the surface tension of an unknown N-LC.

https://dx.doi.org/10.1021/acsami.0c21044
ACS Appl. Mater. Interfaces 2021, 13, 4574−4582

CONCLUSIONS

In this paper, we showed that the addition of chiral ligand-capped Au nanoparticles (Au NPs) to nematic liquid crystals leads to the formation of microlenses. We found that the focal length is the same for the nonpolarized or linearly polarized input beam but is different when left- or right-handed circular polarizers are used. These results show that cholesteric liquid crystal lenses in some extent may be approximated as an integrated Pancharatnam–Berry phase element and a biconvex lens. However, the precise determination of the optical focusing properties needs further theoretical work.

Although the formation of such lenses requires the presence of water that restricts their use compared to those liquid crystal lenses that are enclosed between glass substrates, they have several advantages that make them worthwhile for further studies.

(i) As it was already shown, colloidal nematic liquid crystal microlens arrays can be polymer-stabilized.[61] Based on a similar technique, we achieved preliminary success with polymerizing the LC lens under water such that it maintains its shape even in air after the water is removed. We will also form the gels of the water, which then protects the fluid LC lens inside.

(ii) The microlens has a nanostructure similar to that of the compound eyes of insects; hence, understanding the optics of cholesteric lenses can reveal how insect eyes are formed and how insects can distinguish light polarization states.

(iii) From the shape of the lenses, the helical twisting power of the chiral nanoparticles can be determined using only nanograms of chiral NPs. We specifically found that the helical twisting power of the cholesterol–thiol ligand-capped Au NPs is 400 μm^{-1}.

(iv) Finally, using nanoparticles that are sensitive to external stimuli such as light, electric, and magnetic fields, if their core material is accordingly adjusted, the use of chiral NPs may allow the achievement of possible tunable optical properties for such microlens arrays. Such studies will be carried out in the near future.

ASSOCIATED CONTENT

Supporting Information

The Supporting Information is available free of charge at https://pubs.acs.org/doi/10.1021/acsami.0c21044.

Video demonstrates how the focal length changes when the linear polarization of the incoming light changes to the left and right circularly polarized state (MP4)

AUTHOR INFORMATION

Corresponding Author

Antal Jákli − *Physics Department and Materials Science Graduate Program, Kent State University, Kent, Ohio 44242, United States; Advanced Materials and Liquid Crystal Institute Kent State University, Kent, Ohio 44242, United States;* orcid.org/0000-0001-8627-7606; Email: ajakli@kent.edu

Authors

Kelum Perera − *Physics Department, Kent State University, Kent, Ohio 44242, United States*

Ahlam Nemati − *Advanced Materials and Liquid Crystal Institute Kent State University, Kent, Ohio 44242, United States; Materials Science Graduate Program, Kent State University, Kent, Ohio 44242, United States;* orcid.org/0000-0003-0282-2027

Elizabeth K. Mann − *Physics Department and Materials Science Graduate Program, Kent State University, Kent, Ohio 44242, United States*

Torsten Hegmann − *Advanced Materials and Liquid Crystal Institute Kent State University, Kent, Ohio 44242, United States; Materials Science Graduate Program, Department of Chemistry and Biochemistry, and Brain Health Research Institute, Kent State University, Kent, Ohio 44242, United States;* orcid.org/0000-0002-6664-6598

Complete contact information is available at: https://pubs.acs.org/10.1021/acsami.0c21044

Author Contributions

K.P. carried out physics experiments with directions from E.M. and A.J., A.N. synthesized the chiral nanoparticles, T.H. directed the synthetic work, and A.J. designed the experiments. The manuscript was written through contributions of all authors. All authors have given approval to the final version of the manuscript.

Notes

The authors declare no competing financial interest.

ACKNOWLEDGMENTS

This work was supported by the NSF DMR-1904091 and 1709985. A.J. and K.P. are thankful to Prof. Phil Bos and Mr. Yongle Qi for their helpful discussions about the optics of the lenses.

REFERENCES

(1) Iimura, Y.; Onoe, H.; Takeuchi, S. *CLOSE-PACKED LIQUID-FILLED TUNABLE MICROLENS ARRAY Measurement of Membrane Deformation*. 2014, *2* (c), 1163–1166.

(2) Nose, T.; Masuda, S.; Sato, S.; Li, J.; Chien, L.-C.; Bos, P. J. Effects of Low Polymer Content in a Liquid-Crystal Microlens. *Opt. Lett.* **1997**, *22*, 351.

(3) Naumov, A. F.; Loktev, M. Y.; Guralnik, I. R.; Vdovin, G. Liquid-Crystal Adaptive Lenses with Modal Control. *Opt. Lett.* **1998**, *23*, 992.

(4) Lin, Y. H.; Chen, H. S.; Lin, H. C.; Tsou, Y. S.; Hsu, H. K.; Li, W. Y. Polarizer-Free and Fast Response Microlens Arrays Using Polymer-Stabilized Blue Phase Liquid Crystals. *Appl. Phys. Lett.* **2010**, *96*, 24–27.

(5) Masuda, S.; Takahashi, S.; Nose, T.; Sato, S.; Ito, H. Liquid-Crystal Microlens with a Beam-Steering Function. *Appl. Opt.* **1997**, *36*, 4772.

(6) Akatay, A.; Ataman, C.; Urey, H. High-Resolution Beam Steering Using Microlens Arrays. *Opt. Lett.* **2006**, *31*, 2861.

(7) Lee, J.-H.; Ho, Y.-H.; Chen, K.-Y.; Lin, H.-Y.; Fang, J.-H.; Hsu, S.-C.; Lin, J.-R.; Wei, M.-K. Efficiency Improvement and Image Quality of Organic Light-Emitting Display by Attaching Cylindrical Microlens Arrays. *Opt. Express* **2008**, *16*, 21184.

(8) Hassanfiroozi, A.; Jen, T.; Huang, Y. *Liquid Crystal Lens Array for a 3D Endoscope*. 2014, No. May, 2–6 . DOI: 10.1117/2.1201405.005419.

(9) Li, F.; Chen, S.; Luo, H.; Gao, Y. Curved Micro Lens Array for Bionic Compound Eye. *Optik* **2013**, *124*, 1346–1349.

(10) Park, M.-K.; Lee, H. J.; Park, J.-S.; Kim, M.; Bae, J. M.; Mahmud, I.; Kim, H.-R. Design and Fabrication of Multi-Focusing Microlens Array with Different Numerical Apertures by Using Thermal Reflow Method. *J. Opt. Soc. Korea* **2014**, *18*, 71–77.

(11) Wu, M. H.; Park, C.; Whitesides, G. M. Fabrication of Arrays of Microlenses with Controlled Profiles Using Gray-Scale Microlens Projection Photolithography. *Langmuir* **2002**, *18*, 9312–9318.

(12) Wu, H.; Hu, W.; Hu, H.; Lin, X.; Zhu, G.; Choi, J.-W.; Chigrinov, V.; Lu, Y. Arbitrary Photo-Patterning in Liquid Crystal Alignments Using DMD Based Lithography System. *Opt. Express* **2012**, *20*, 16684.
(13) Guo, Y.; Jiang, M.; Peng, C.; Sun, K.; Yaroshchuk, O.; Lavrentovich, O.; Wei, Q. H. High-Resolution and High-Throughput Plasmonic Photopatterning of Complex Molecular Orientations in Liquid Crystals. *Adv. Mater.* **2016**, *28*, 2353−2358.
(14) Jiang, M.; Guo, Y.; Yu, H.; Zhou, Z.; Turiv, T.; Lavrentovich, O. D. *Low f -Number Diffraction-Limited Pancharatnam − Berry Microlenses Enabled by Plasmonic Photopatterning of Liquid Crystal Polymers*. 2019, *31*, 1−7. DOI: 10.1002/adma.201808028.
(15) He, Z.; Lee, Y.-H.; Chen, R.; Chanda, D.; Wu, S.-T. Switchable Pancharatnam−Berry Microlens Array with Nano-Imprinted Liquid Crystal Alignment. *Opt. Lett.* **2018**, *43*, 5062.
(16) Ishii, Y.; Koike, S.; Arai, Y.; Ando, Y. Ink-Jet Fabrication of Polymer Microlens for Optical-I/O Chip Packaging. *Jpn. J. Appl. Phys.* **2000**, *39*, 1490−1493.
(17) Nussbaum, P.; Völkel, R.; Herzig, H. P.; Eisner, M.; Haselbeck, S. Design, Fabrication and Testing of Microlens Arrays for Sensors and Microsystems. *Pure. Appl. Opt.* **1997**, *6*, 617−636.
(18) Masuda, S.; Honma, M.; Nose, T.; Sato, S. Influence of Elastic Constants on the Optical Properties of Liquid Crystal Microlenses. *Jpn. J. Appl. Phys.* **1997**, *36*, 2765−2770.
(19) Ye, M.; Sato, S. Transient Properties of a Liquid-Crystal Microlens. *Jpn. J. Appl. Phys.* **2001**, *40*, 6012−6016.
(20) Honma, M.; Nose, T.; Sato, S. Improvement of Aberration Properties of Liquid Crystal Microlenses Using the Stacked Electrode Structure. *Jpn. J. Appl. Phys.* **2001**, *40*, 1322−1327.
(21) Pishnyak, O.; Sato, S.; Lavrentovich, O. D. Electrically Tunable Lens Based on a Dual-Frequency Nematic Liquid Crystal. *Appl. Opt.* **2006**, *45*, 4576−4582.
(22) Xu, S.; Li, Y.; Liu, Y.; Sun, J.; Ren, H.; Wu, S. T. Fast-Response Liquid Crystal Microlens. *Micromachines* **2014**, *5*, 300−324.
(23) Lin, Y.-H.; Chen, H.-S.; Chen, M.-S. Electrically Tunable Liquid Crystal Lenses and Applications. *Mol. Cryst. Liq. Cryst.* **2014**, *596*, 12−21.
(24) Ma, Y.; Tam, A. M. W.; Gan, X. T.; Shi, L. Y.; Srivastava, A. K.; Chigrinov, V. G.; Kwok, H. S.; Zhao, J. L. Fast Switching Ferroelectric Liquid Crystal Pancharatnam-Berry Lens. *Opt. Express* **2019**, *27*, 10079.
(25) Yu, H.; Zhou, Z.; Qi, Y.; Zhang, X.; Wei, Q. H. Pancharatnam−Berry Optical Lenses. *J. Opt. Soc. Am. B* **2019**, *36*, D107−D111.
(26) Gao, K.; Cheng, H.-H.; Bhowmik, A.; McGinty, C.; Bos, P. Nonmechanical Zoom Lens Based on the Pancharatnam Phase Effect. *Appl. Opt.* **2016**, *55*, 1145.
(27) Berry, M. V. The Adiabatic Phase and Pancharatnam's Phase for Polarized Light. *J. Mod. Opt.* **1987**, *34*, 1401−1407.
(28) Bomzon, Z.; Kleiner, V.; Hasman, E. Pancharatnam−Berry Phase in Space-Variant Polarization-State Manipulations with Subwavelength Gratings. *Opt. Lett.* **2001**, *26*, 1424.
(29) Marrucci, L.; Manzo, C.; Paparo, D. Pancharatnam-Berry Phase Optical Elements for Wave Front Shaping in the Visible Domain: Switchable Helical Mode Generation. *Appl. Phys. Lett.* **2006**, *88*, 221102−221104.
(30) Lee, Y.-H.; Tan, G.; Zhan, T.; Weng, Y.; Liu, G.; Gou, F.; Peng, F.; Tabiryan, N. V.; Gauza, S.; Wu, S.-T. Recent Progress in Pancharatnam−Berry Phase Optical Elements and the Applications for Virtual/Augmented Realities. *Opt. Data Process. Storage* **2017**, *3*, 79−88.
(31) Jin, J.; Zhang, X.; Gao, P.; Luo, J.; Zhang, Z.; Li, X.; Ma, X. Ultrathin Planar Microlens Arrays Based on Geometric Metasurface. *Ann. Physik.* **2018**, *530*, 1−6.
(32) Sato, S. Liquid-Crystal Lens-Cells with Variable Focal Length. *Jpn. J. Appl. Phys.* **1979**, *18*, 1679−1684.
(33) Patel, J. S.; Rastani, K. Electrically Controlled Polarization-Independent Liquid Crystal Fresnel Lens Arrays. *Opt. Lett.* **1991**, *16*, 532−534.
(34) Lee, J.-H.; Beak, J.-H.; Kim, Y.; Lee, Y.-J.; Kim, J.-H.; Yu, C.-J. Switchable Reflective Lens Based on Cholesteric Liquid Crystal. *Opt. Express* **2014**, *22*, 9081.
(35) Kim, Y. H.; Jeong, H. S.; Kim, J. H.; Yoon, E. K.; Yoon, D. K.; Jung, H.-T. Fabrication of Two-Dimensional Dimple and Conical Microlens Arrays from a Highly Periodic Toroidal-Shaped Liquid Crystal Defect Array. *J. Mater. Chem.* **2010**, *20*, 6557.
(36) Serra, F.; Gharbi, M. A.; Luo, Y.; Liu, I. B.; Bade, N. D.; Kamien, R. D.; Yang, S.; Stebe, K. J. Curvature-Driven, One-Step Assembly of Reconfigurable Smectic Liquid Crystal "Compound Eye" Lenses. *Adv. Opt. Mater.* **2015**, *3*, 1287−1292.
(37) Ma, L. L.; Wu, S. B.; Hu, W.; Liu, C.; Chen, P.; Qian, H.; Wang, Y.; Chi, L.; Lu, Y. Q. Self-Assembled Asymmetric Microlenses for Four-Dimensional Visual Imaging. *ACS Nano* **2019**, *13*, 13709−13715.
(38) Bayon, C.; Agez, G.; Mitov, M. Lab on a Chip Liquid Crystal Microlenses †. *Lab Chip* **2014**, *14*, 2063−2071.
(39) Popov, P.; Honaker, L. W.; Mirheydari, M.; Mann, E. K.; Jákli, A. Chiral Nematic Liquid Crystal Microlenses/639/301/639/624/123/132/124/128/129 Article. *Sci. Rep.* **2017**, *7*, 1603.
(40) Ke, Y.; Liu, Y.; Zhou, J.; Liu, Y.; Luo, H.; Wen, S. Optical Integration of Pancharatnam-Berry Phase Lens and Dynamical Phase Lens. *Appl. Phys. Lett.* **2016**, *108*, 101102.
(41) Li, Y.; Liu, Y.; Luo, D. A Photo-Switchable and Photo-Tunable Microlens Based on Chiral Liquid Crystals. *J. Mater. Chem. C* **2019**, *7*, 15166−15170.
(42) Brown, G. H.; Wolken, J. J. *Liquid Crystals and Biological Structures*; Academic Press: New York, 1979.
(43) Bouligand, Y.; Soyer, M. O.; Puiseux-Dao, S. La Structure Fibrillaire et l'orientation Des Chromosomes Chez Les Dinoflagell?? *Chromosoma* **1968**, *24*, 251−287.
(44) Bouligand, Y. Theory of Microtomy Artefacts in Arthropod Cuticle. *Tissue Cell* **1986**, *18*, 621−643.
(45) Glushchenko, A.; Cheon, C. I.; West, J.; Li, F.; Büyüktanir, E.; Reznikov, Y.; Buchnev, A. Ferroelectric Particles in Liquid Crystals: Recent Frontiers. *Mol. Cryst. Liq. Cryst.* **2006**, *453*, 227−237.
(46) Kurochkin, O.; Buchnev, O.; Iljin, A.; Park, S. K.; Kwon, S. B.; Grabar, O.; Reznikov, Y. A Colloid of Ferroelectric Nanoparticles in a Cholesteric Liquid Crystal. *J. Opt. A Pure Appl. Opt.* **2009**, *11*, No. 024003.
(47) Nayek, P.; Li, G. Superior Electro-Optic Response in Multiferroic Bismuth Ferrite Nanoparticle Doped Nematic Liquid Crystal Device. *Sci. Rep.* **2015**, *5*, 1−9.
(48) Gutierrez-Cuevas, K. G.; Wang, L.; Zheng, Z. G.; Bisoyi, H. K.; Li, G.; Tan, L. S.; Vaia, R. A.; Li, Q. Frequency-Driven Self-Organized Helical Superstructures Loaded with Mesogen-Grafted Silica Nanoparticles. *Angew. Chem., Int. Ed.* **2016**, *55*, 13090−13094.
(49) Choudhary, A.; Singh, G.; Biradar, A. M. Advances in Gold Nanoparticle-Liquid Crystal Composites. *Nanoscale* **2014**, *6*, 7743−7756.
(50) Vardanyan, K. K.; Walton, R. D.; Bubb, D. M. A. Liquid Crystal Composites with a High Percentage of Gold Nanoparticles. *Liq. Cryst.* **2011**, *38*, 1279−1287.
(51) Zhang, G.; Chen, X.; Zhao, J.; Chai, Y.; Zhuang, W.; Wang, L. Electrophoretic Deposition of Silver Nanoparticles in Lamellar Lyotropic Liquid Crystal. *Mater. Lett.* **2006**, *60*, 2889−2892.
(52) Mori, T.; Sharma, A.; Hegmann, T. Significant Enhancement of the Chiral Correlation Length in Nematic Liquid Crystals by Gold Nanoparticle Surfaces Featuring Axially Chiral Binaphthyl Ligands. *ACS Nano* **2016**, *10*, 1552−1564.
(53) Nemati, A.; Shadpour, S.; Querciagrossa, L.; Mori, T.; Zannoni, C.; Hegmann, T. Highly Sensitive, Tunable Chirality Amplification through Space Visualized for Gold Nanorods Capped with Axially Chiral Binaphthyl Derivatives. *ACS Nano* **2019**, *13*, 10312−10326.
(54) Ostovar Pour, S.; Rocks, L.; Faulds, K.; Graham, D.; Parchaňský, V.; Bouř, P.; Blanch, E. W. Through-Space Transfer of Chiral Information Mediated by a Plasmonic Nanomaterial. *Nat. Chem.* **2015**, *7*, 591−596.

https://dx.doi.org/10.1021/acsami.0c21044
ACS Appl. Mater. Interfaces 2021, 13, 4574−4582

(55) Guerrero-Martínez, A.; Alonso-Gómez, J. L.; Auguié, B.; Cid, M. M.; Liz-Marzán, L. M. From Individual to Collective Chirality in Metal Nanoparticles. *Nano Today* **2011**, *6*, 381−400.
(56) Guerrero-Martínez, A.; Auguié, B.; Alonso-Gómez, J. L.; Džolič, Z.; Gómez-Graña, S.; Žinić, M.; Cid, M. M.; Liz-Marzán, L. M. Intense Optical Activity from Three-Dimensional Chiral Ordering of Plasmonic Nanoantennas. *Angew. Chem., Int. Ed.* **2011**, *50*, 5499−5503.
(57) Nemati, A.; Shadpour, S.; Querciagrossa, L.; Li, L.; Mori, T.; Gao, M.; Zannoni, C.; Hegmann, T. Chirality Amplification by Desymmetrization of Chiral Ligand-Capped Nanoparticles to Nanorods Quantified in Soft Condensed Matter. *Nat. Commun.* **2018**, *9*, 1−13.
(58) Gupta, V. K.; Skaife, J. J.; Dubrovsky, T. B.; Abbott, N. L. Optical Amplification of Ligand-Receptor Binding Using Liquid Crystals. *Science* **1998**, *279*, 2077−2080.
(59) Popov, P.; Mann, E. K.; Jákli, A. Accurate Optical Detection of Amphiphiles at Liquid-Crystal-Water Interfaces. *Phys. Rev. Appl.* **2014**, *1*, No. 034003.
(60) Popov, P.; Mann, E. K.; Jákli, A. Thermotropic Liquid Crystal Films for Biosensors and Beyond. *J. Mater. Chem. B* **2017**, *5*, 5061−5078.
(61) Ren, H.; Xu, S.; Wu, S.-T. Polymer-Stabilized Liquid Crystal Microlens Array with Large Dynamic Range and Fast Response Time. *Opt. Lett.* **2013**, *38*, 3144.
(62) Yu, N.; Genevet, P.; Kats, M. A.; Aieta, F.; Tetienne, J.-P.; Capasso, F.; Gaburro, Z. Light Propagation with Phase Reflection and Refraction. *Science* **2011**, *334*, 333−337.
(63) Jiang, M.; Yu, H.; Feng, X.; Guo, Y.; Chaganava, I.; Turiv, T.; Lavrentovich, O. D.; Wei, Q. H. Liquid Crystal Pancharatnam−Berry Micro-Optical Elements for Laser Beam Shaping. *Adv. Opt. Mater.* **2018**, *6*, 1−7.
(64) Gao, K.; Cheng, H.; Bhowmik, A. K.; Bos, P. J. Thin-Film Pancharatnam Lens with Low f-Number and High Quality. *Opt. Express* **2015**, *23*, 26086−26094.

https://dx.doi.org/10.1021/acsami.0c21044
ACS Appl. Mater. Interfaces 2021, 13, 4574−4582